

CONFERENCES AND SYMPOSIA

Scientific Session of the Division of General Physics and Astronomy of the Russian Academy of Sciences (27 September 1995)

On 27 September 1995, in the E K Zavoiskiĭ Institute of Physics and Technology at the Kazan' Science Centre of the Russian Academy of Sciences, a Scientific Session of the Department of General Physics and Astronomy of the Russian Academy of Sciences, devoted to the 50th Anniversary of the Institute, was held. The talks presented were the following:

(1) **K M Salikhov and Yu E Kandrashkin** (Institute of Physics and Technology at the Kazan' Science Centre of the Russian Academy of Sciences) *Spin coherence effects in the EPR spectroscopy of separated charges in a photosynthesis reaction centre*;

(2) **A A Bukharaev** (Institute of Physics and Technology at the Kazan' Science Centre of the Russian Academy of Sciences) *Scanning tunnelling and atomic force microscopy of surfaces modified by ion and laser beams*;

(3) **V E Kataev, Yu S Greznev, B Z Rameev, E F Kukovitskiĭ, G B Teitel'baum** (Institute of Physics and Technology at the Kazan' Science Centre of the Russian Academy of Sciences), **M Breuer, N Knauf** (II Institute of Physics at Cologne University, FRG) *An EPR study of the density of states and effective coupling constant in* La_2CuO_4 *doped with* Sr *or* Ba.

(4) **I B Khaibullin** *Radiation-stimulated processes in solids*;

(5) **I V Ovchinnikov, Yu G Galyametdinov** *Metal-containing magnetic liquid crystals*;

(6) **G G Khaliullin, I A Garifullin, Yu V Goryunov** *Spin-wave resonance in a superconductor with paramagnetic impurities*.

The first three talks are reviewed briefly below.

PACS numbers: **76.30.–v**, 87.22.Fy

Spin coherence effects in the EPR spectroscopy of separated charges in a photosynthesis reaction centre

K M Salikhov and Yu E Kandrashkin

1. Introduction

In studying the initial charge separation stages of the photosynthesis process, electron paramagnetic resonance (EPR) methods have proved very useful (see [1], for example). EPR spectroscopy provides unique information on the spin dynamics in electron-hole pairs in the reaction centre of the photosynthesis apparatus, as well as yielding magneto-resonance parameters such as the spin-spin, dipole-dipole, and exchange interactions in these pairs. In its turn, if one knows the magnitude of the dipole-dipole interaction, for example, the distance between the separated charges and important information about the structure of the reaction centre can be obtained [2].

EPR spectroscopy of electron-hole pairs in the reaction centre shows a number of remarkable features related to the fact that the pair spins are out of thermodynamic equilibrium initially and there is a mutual correlation between the electron and hole spin states. An elementary electron transfer event at the primary photosynthesis stage occurs on a pico- or subnanosecond scale too short for the electron spins to change their states [3]. As a result, the spins of the electron-hole pairs in the reaction centre inherit the singlet nature of the preceding singlet excited state of the chlorophyll molecule. The singlet state is not stationary for the separated charges in the centre, and in the pairs under consideration radiationless singlet-triplet transitions take place. The dynamics of pair spins manifests itself in a characteristic way in EPR spectroscopy.

At the first photosynthesis stage, the electron hops from one acceptor to another and a succession of electron-hole pairs forms, in which the spin state of one pair is transmitted to the next pair. The electron spins in the pair are coherent, i.e., in the E representation some of the off-diagonal density matrix elements are nonzero. It is this spin coherency of the electron-hole pairs and its transfer along the succession of the pairs which determine the photosynthesis reaction EPR features discussed in this report. The report is a summary of our theoretical work [4 – 6] on spin coherence effects in time-resolved EPR experiments involving photosynthetic systems.

2. The model

Consider a pair with a spin Hamiltonian of the form [5]

$$H_0 = \hbar\left[\omega_A S_{Az} + \omega_B S_{Bz} + (-2J + 2d)\, S_{Az} S_{Bz} - (2J + d) \times (S_{Ax} S_{Bx} + S_{Ay} S_{By})\right], \quad (1)$$

where the first two terms describe the Zeeman interactions of the spins with the external permanent magnetic field, and the last terms account for the exchange and dipole-dipole interactions in the pair. The primary pair forms in a singlet state. The average lifetime of the primary pair is τ_0. The subsequent (second) pair has a spin Hamiltonian of the same form (1) as the primary pair but with different values of the magneto-resonance parameters. Switching on the RF (more specifically, SHF) field adds to the Hamiltonian the term

$$H_1 = \hbar\omega_1 (S_{Ax} + S_{Bx}), \quad (2)$$

Uspekhi Fizicheskikh Nauk **166** (2) 207–216 (1996)
Translated by E G Strel'chenko, edited by A Radzig

where $\omega_1 = \gamma B_1$, B_1 is the RF field induction, and γ, the electron gyromagnetic ratio.

The following experimental EPR signal models has been analysed:

M o d e l A: The time-resolved response to a continuous nonsaturating RF field of electron-hole pairs produced by a short (nanosecond) laser pulse. The EPR signal intensity is calculated as a function of time since the pulse.

M o d e l B: At the initial point in time, singlet electron-hole pairs are created. After a time delay τ, a $\pi/2$ RF pulse is applied, and the free induction signal (FIS) is detected. The FIS intensity is calculated as a function of two time intervals, the RF pulse time delay τ, and the time t after RF pulse generation.

M o d e l C: At the initial point in time, singlet electron-hole pairs are created. After a time delay τ, a succession of two RF pulses is applied, and the primary spin echo (ESE) signal is detected. The ESE signal intensity is calculated as a function of two time intervals, the RF pulse time delay τ, and the time t after the generation of the second RF pulse.

M o d e l D: At the initial point in time, singlet electron-hole pairs are created. With an average lifetime τ_0, this pair transforms into another pair. The time-resolved response of this pair succession to continuous nonsaturating RF field is calculated.

3. Results

From analytical and numerical calculations, the following results have been obtained.

In model A, all EPR lines of a pair experience quantum intensity beats [4, 5]:

$$I \propto \sin^2(Rt), \qquad R^2 = (\omega_A - \omega_B)^2 + (2J + d)^2 . \tag{3}$$

The beats are due to the coherence in the spin states of the pairs. A detailed discussion of this question can be found elsewhere [4, 5, 7, 8]. The EPR intensity beats for spin-correlated pairs predicted in these studies have been confirmed experimentally for the reaction centre of the photosynthesis apparatus [9].

In model B, a remarkable FIS result is found. For the spin-correlated pairs considered, the free induction signal does not appear immediately after the $\pi/2$ RF pulse, but first increases from zero and then passes through a maximum (Fig. 1a, b). It is seen from the figures that the FIS behaves like a primary spin echo signal formed by two RF pulses in a spin system that was in thermodynamic equilibrium prior to the experiment [6]. The explanation for this unusual FIS behaviour is that the laser pulse creates coherent-state electron-hole pairs. In this model, the FIS may be thought of as the spin echo signal produced by a laser pulse and an RF pulse, in that order. The former produces pairs in the singlet — i.e., spin- correlated — state. The signal may therefore be viewed as an analogue of a solid-state spin-dipole echo [10]: suitably tailored alternate-field pulses create dipole order in the spin system, and after some delay a FIS observation pulse is applied.

For spin-correlated pairs, an ordinary echo may also be observed (model C). Fig. 2 shows some of our results (see Ref. [6] for more details). Two features of the ESE signals of spin-correlated pairs should be noted:

(1) the maximum of the ESE signal does not occur exactly at the time $2t$ after the first RF pulse (t is the time separation between two RF pulses);

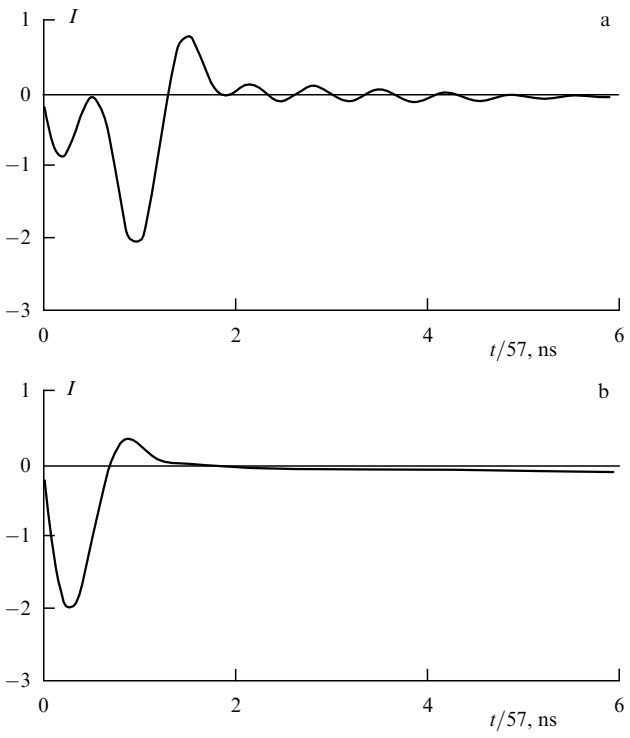

Figure 1. Free induction signal for $\tau = 28.5$ ns (a) and $t = 228$ ns (b). The FIS is clearly seen to follow primary echo behaviour: just after the RF pulse, the signal is zero, then it increases to a maximum and starts to decrease. Comparing spectra for various laser-RF pulse separations τ reveals a spin evolution. Calculation parameters are typical for the EPR spectrometer X-range: $\omega_A/\gamma = 3000$ G, $\omega_B/\gamma = 3010$ G, $J/\gamma = 1$ G, $d = 0$. Time t is in units of 57 ns; intensity I, in arbitrary units.

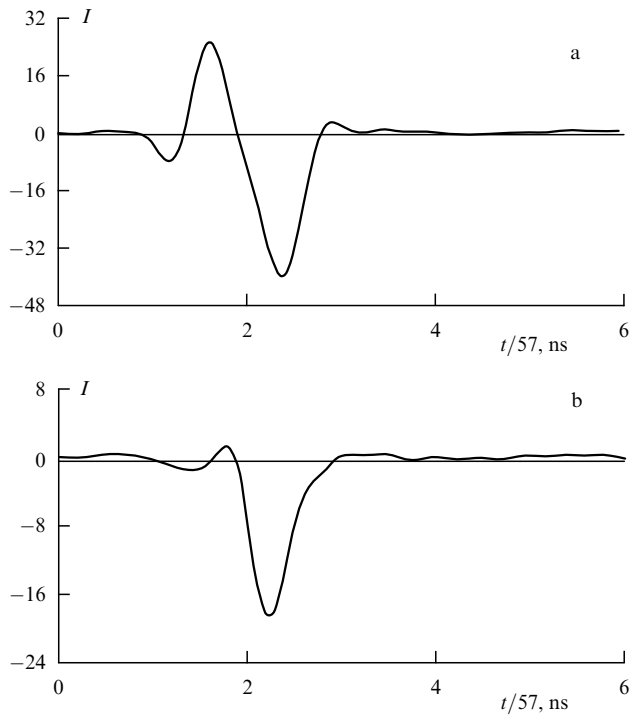

Figure 2. ESE signal at $\tau = 28.5$ ns (a) and $\tau = 228$ ns (b). The time separation between two RF signals is $t = 114$ ns. It is clearly seen that the maximum of the ESE amplitude occurs at time t' different from t. Calculation parameters are the same as in Fig. 1.

(2) the phase of the ESE signal for spin-correlated pairs differs from what is expected for spin pairs in thermodynamic equilibrium. The ESE phase of correlated pairs depends on the nature (degree) of spin excitation by the echo-forming RF pulses. For example, in the complete excitation case the shift in the ESE phase of spin-correlated pairs is close to $\pi/2$ relative to that of equilibrium spin pairs.

As mentioned earlier, at primary photosynthesis stages, not a single pair but a succession of electron-hole pairs forms. For this reason, time-resolved EPR spectra of two successive pairs have been calculated (model D). Some of the results are given in Figs 3 and 4 [11]. As in the single-pair situation, two successive pairs exhibit quantum beats in their EPR lines intensities. However, the intensity of the second pair has a different time dependence than it would be in the absence of the first pair. It is shown that the quantum beats for the second pair exhibit a phase shift. This shift appears even when, due to the relatively short lifetime of the first pair, its EPR spectrum is impossible to detect. Therefore the phase shift in EPR intensity oscillations of the radical pair may serve as a criterion for the existence of the preceding pair and enables the resonance parameters of this pair to be estimated.

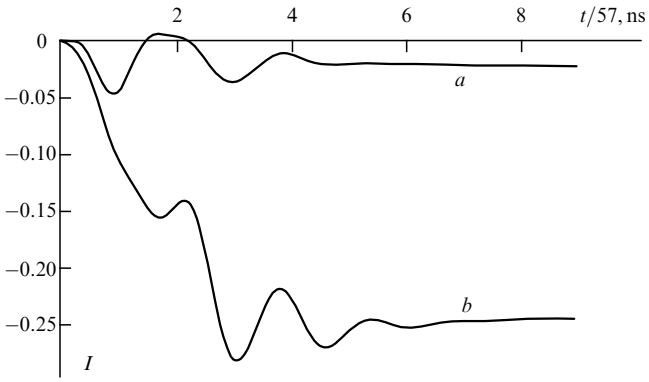

Figure 3. Time-resolved EPR spectrum for two independent radical pairs (*a*) and two successive pairs (*b*). In both cases the first pair forms right after the laser pulse and has an average lifetime $\tau_0 = 57$ ns, whereas the second pair emerges with a chemical reaction rate constant $k = 1/\tau_0$. The spectra are seen to differ greatly. There is a noticeable phase shift of EPR intensity beats for the successive pair compared to the spectrum of an independently created pair. Calculation parameters are typical for the EPR spectrometer X-range: for the first pair, $\omega_A/\gamma = 3003$ G, $\omega_B/\gamma = 3005$ G, $J/\gamma = 1$ G, $d = 0$; for the second pair, $\omega_A/\gamma = 3002$ G, $\omega_B/\gamma = 3006$ G, $J/\gamma = 0.1$ G, $d = 0$.

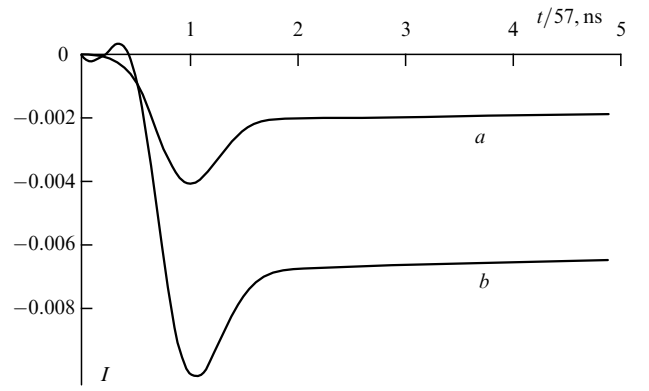

Figure 4. Time-resolved EPR spectrum for two independent radical pairs (*a*) and two successive pairs (*b*). In both cases the first pair forms right after the laser pulse and has an average lifetime of $\tau_0 = 57$ ns, whereas the second pair emerges with a chemical reaction rate constant $k = 1/\tau_0$. Unlike Fig. 3, the chemical reaction rate constant is an order of magnitude larger, so only the spectra from the second pairs are actually seen. Nevertheless, the phase of EPR intensity beats is shifted noticeably relative to the spectrum of an independently created pair. Calculation parameters are typical for the EPR spectrometer X-range: for the first pair, $\omega_A/\gamma = 3003$ G, $\omega_B/\gamma = 3005$ G, $J/\gamma = 1$ G, $d = 0$; for the second pair, $\omega_A/\gamma = 3002$ G, $\omega_B/\gamma = 3006$ G, $J/\gamma = 0.1$ G, $d = 0$.

References

1. *Advanced EPR. Applications in Biology and Biochemistry* (Ed. A J Hoff) (Amsterdam: Elsevier, 1989)
2. Fuchsle G et al. *Biochimica et Biophysica Acta* **1142** 23 (1993)
3. Norris J R, Schiffer M *Chemical and Engineering News* **68** (31) 22 (1990)
4. Salikhov K M *Usp. Fiz. Nauk* **160** (4)77 (1990) [*Sov. Phys. Usp.* **33** (4) 299 (1990)]
5. Salikhov K M, Bock C H, Shtelik D *Applied Magnetic Resonance* **1** 195 (1990)
6. Salikhov K M, Kandrashkin Yu E, Salikhov A K *Applied Magnetic Resonance* **3** 199 (1992)
7. Bittl R, Schulten K *Chem. Phys. Lett.* **173** (4) 387 (1991)
8. Bittl R et al. *Chem. Phys. Lett.* **226** 349 (1994)
9. Kothe G et al. in *Spin Chemistry* (Ed. Y J I'Haya) (Tokyo, 1991) pp. 420 – 434
10. Jeener J, Broekaert P *Phys. Rev.* **157** (2) 232 (1967)
11. 11. Kandrashkin Yu E, Salikhov K M, Shtelik D (to be published)

PACS numbers: 07.79.Cz, 07.79.Lh, 42.62.Hk

Scanning tunnelling and atomic force microscopy of surfaces modified by ion and laser beams

A A Bukharaev

1. Introduction

Scanning tunnelling and atomic force microscopes (STMs and AFMs) are finding increasing use in surface studies. This is explained by a number of unique advantages they offer, including a three-dimensional image of the surface; high (up to atomic scale) spatial resolution, not only in a superhigh vacuum but also in air; the possibility of studies both in a vacuum and in a liquid or gaseous medium, and, finally, working in the scanning tunnelling spectroscopy (STS) regime, which enables data on the distribution of electronic characteristics at the surface of a solid to be obtained.

STMs allow the investigations of the surface of a conducting medium. However, STM results obtained in the atmosphere should be regarded with some caution because of the strong effect of the adsorbed layers covering the surface in the air [1, 2]. Unlike STMs, AFMs provide high-resolution three-dimensional images of both conducting and nonconducting surfaces, but the surface distribution of electronic characteristics cannot as yet be studied with the same resolution as given by STMs.

This report presents the results obtained by the tunnelling microscopy group of the Kazan' Institute of Physics and Technology of RAS in STM and AFM studies on laser-modified Si and quartz-glass surfaces previously treated by ion etching.

In these studies, much attention has been given to the specifics of STM studies in air, notably to the effect of

adsorbed layers, whether natural or induced by the electric field of the STM needle, on STM/STS results. Besides, part of the work is concerned with the appearance (and methods for the elimination) of surface image distortions arising from the finite sizes of the STM and AFM needles.

The primary research objectives were to assess the reliability of STM-AFM data; to develop methods for reducing or eliminating possible image distortions; and to investigate processes at the implanted surface subject to a powerful laser pulse, from the viewpoint of using a given material in high-bit-density optical information record and storage.

The objects for the study were not chosen in a fortuitous manner. It is known that in certain ion implantation regimes the surface layer of Si becomes amorphous, the result being that the optical absorption coefficient of Si in the 1-μm range increases from 10^2 to 10^4 cm^{-1}. A similar effect was observed by us earlier [3] for the implantation of optical glasses by metal ions. The optical absorption coefficient of colourless optical glass in the visible and UV regions increased to 10^5 cm^{-1} after ion bombardment. In that case, the increase in the absorption coefficient is due to the formation of 5 – 100-nm metal particles in the implanted layer [3].

When such a medium is subject to a laser pulse, most of the energy is released in a thin high-absorptive implanted layer, thus producing a radiation sensitive material of good promise for optical information recording [4].

2. Experimental features of STM and AFM surface studies

Our investigations [1, 2] show that a major condition of the reliability of STM or STS data on the microtopography and electronic properties of Si requires that there be a tunnel contact between the STM needle and the Si surface. For an STM in air, such a contact may be produced by a special multistage passivation involving (i) the removal of the oxide layer and surface-contaminating hydrocarbons, and (ii) the hydrogen saturation of the active chemical bondings of the surface Si atoms [1]. Although a hydrogenated Si surface does not oxidise for several hours in air, the electric field of the STM needle may depassivate it as well as cause an intense deposition of adsorbates from the air onto the Si surface and the STM needle. This deteriorates considerably the quality of the STM image, as a consequence of the change in electron transport mechanism (Fig. 1). Our special studies [1, 2] indicated overbarrier Schottky emission as one of the mechanisms capable of satisfactorily explaining the electron transport between the STM needle and the Si surface, both coated by water and hydrocarbon molecules adsorbed from the air. The basic method for monitoring the conduction mechanism in the STM needle–surface gap and inspecting the quality of surface cleaning from the adsorbed contaminates is to detect the STM current for various needle-surface distances [1, 2]. Stimulated adsorption can be prevented by carrying STM measurements in a pure neutral-gas environment.

Passivation of Si surface also results from high-dose iron-group ion implantation [5]. A thin metal-silicide layer thus produced protects Si from becoming oxidised, allowing high-quality STM images after years of keeping samples in air.

An ion- or laser-exposed surface generally develops a microstructure whose roughnesses may be of a comparable size to the needles. Since STM and AFM images are essentially convolutions of the images of the surface and the probing needle, this leads to considerable deviations of the experimental images from the real ones. In this connection, a problem arises as to how to estimate the STM and AFM image distortions due to the finite needle size. Computer imaging simulation has shown that knowing the real shape of the STM/AFM needle allows one to assess the reliability of images of surfaces with a developed microrelief [6].

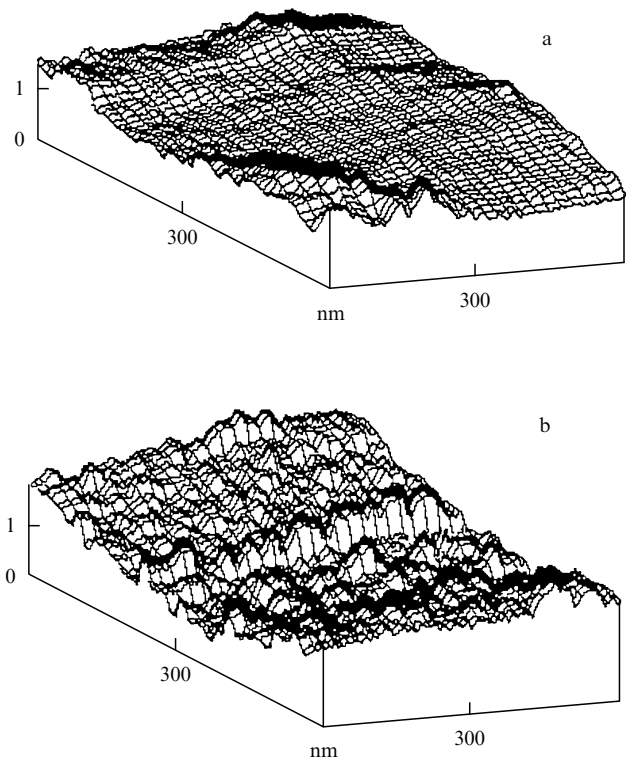

Figure 1. STM image of Si surface immediately after passivation (a), and after 40-min air exposure (b) in the electric field of the STM needle.

It would be most interesting, in our view, to try to deconvolve the obtained image, i.e., to solve the problem inverse to the convolution of the needle and surface images. Knowing the actual needle shape (from electronic microscopy, for example), the experimental image can be brought much closer to the real one. Conversely, using a sample with roughnesses of predetermined shape and size preliminarily produced on it, the image of the actual scanning STM needle can be reproduced. With the needle shape and size thus obtained, surfaces of unknown relief can be studied and, via the deconvolution procedure, AFM image distortions eliminated.

An original computer deconvolution method we proposed in Ref. [7] reduces significantly the needle-shape-related distortions and, for a prescribed microrelief, enables the image of the probe needle tip to be obtained. Fig. 2 illustrates the computer realisation of the method for a hemispheric surface protrusion imaged by a pyramidal AFM needle. It is clearly seen that after deconvolution the corrected AFM image (Fig. 2c) is much closer to the original one. Given the size of the hemisphere, in the same way the deconvolution of the images of the hemispheric protrusion and the AFM needle (Fig. 2b) yields the image of the AFM needle tip (Fig. 2d). If the scanning needle touches all points of the surface, the method eliminates all the distortions arising from the finite size and the shape of the needle [7].

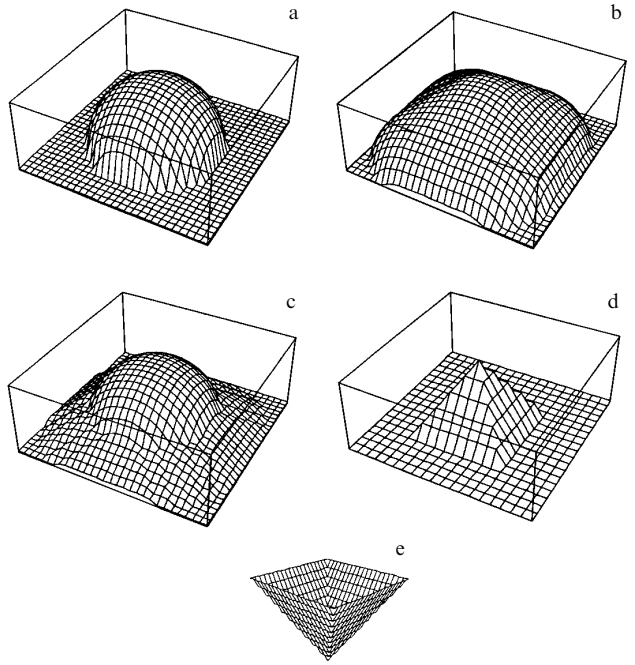

Figure 2. Computer correction for the distortion of the AFM image of a hemispheric protrusion, and AFM-needle shape determination via the deconvolution method: (a) initial surface, (b) its AFM image, (c) deconvolution-corrected AFM image, (d) AFM needle image obtained from (b) by the deconvolution method, (e) shape of the needle used in obtaining the AFM image (b).

The STM used was developed by the KFTI tunnelling microscopy group [8, 9]. Its distinguishing feature is that one and the same portion of the surface yields a dc-regime relief image and the distribution of electronic characteristics simultaneously. In the latter case, scanning each of the 128×64 surface points involves a 100-ms break of the STM feedback and a 50-ms measurement of the current-voltage characteristic (CVC), the latter reflecting the electronic properties of the Si area under the STM needle. To secure the required measuring rate, the CVCs are mapped via the integral parameter $Q = \int |I(V)|\,\mathrm{d}V$. As shown in Refs [8, 9], an increase in Q corresponds to an increase in the conductivity in the semiconductor surface layer due to (i) recrystallisation of the amorphous silicon on heating and (ii) the electroactivation of the implanted impurity. The image characterising the surface distribution of conductivity is obtained in the same way as the ordinary dc-regime STM image, except that the quantity Z describing the relief height at a given point is replaced by the Q value at this point.

In both silicon and quartz-glass surface imaging, the Zelenograd 'Nanotekhnologiya — MDT' atomic-strength microscope P4-SPM was used.

Periodic structures were obtained [10] by two-beam holography with the use of a pulsed ruby laser. After a single 10-ns exposure to two (simultaneous) coherent laser beams, an interference light field formed at the sample surface. In the intensity-modulated field, spatially nonuniform surface heating with concomitant nonuniform melting, evaporation, or recrystallisation took place, with the result that the interference pattern persisted after the pulse, either as a periodic relief or a periodic variation of surface conductivity.

The samples used were Si (111) single-crystal plates KEF-4.5 implanted with 30-keV Sb^+ ions at doses above the amorphisation threshold, and polished plates of optical quartz glass implanted with Fe^+ ions (40 keV, 4×10^{17} ion$\times$ cm^{-2}). Prior to STM measurements, the Si samples were cleaned and passivated by hydrogenating in a dry nitrogen atmosphere as described in [1].

3. Microtopography and electronic properties of implanted semiconductors and glasses following pulsed interference laser exposure

When implanted Si or glass were subjected to a pulsed interference light field, one-dimensional, submicron periodic structures (lattices) generally formed on their surfaces, whose period was described fairly well by the familiar expression $d = \lambda/[2\sin(\alpha/2)]$, where λ is the laser wavelength, and α, the angle between the beams incident onto the surface [9].

Comparison of silicon STM and STS images showed that, for energy densities above 1 J cm^{-2}, STM lattice images with a relief height of about 40 nm were seen, although no marked changes in the parameter Q were observed in this portion of the surface. In this case the large-depth evaporation of Si and the complete recrystallisation of the whole of the surface apparently combine to form a microrelief with practically constant conductivity along the surface. At a density of about 1 J cm^{-2}, simultaneous STM and Q periodic structure images were usually observed, STM protrusions corresponding to high-conductivity surface portions. Finally, for incident radiation densities below 1 J cm^{-2}, virtually no STM lattices were visible, whereas in the Q image a distinct 0.9-μm-periodic structure appeared [10]. In the latter case we believe that rather than Si evaporation, local recrystallisation of the amorphous surface layer of Si at light field energy antinodes occurs ('interference laser annealing'). Since the density of the implantation-amorphised Si is only by 2 – 3% lower than for crystalline Si, the recrystallisation of the 20-nm amorphous layer should not produce a noticeable microrelief.

In the central portion of some of the holographic Si-surface lattices, two-dimensional periodic structures were detected by both AFM and STM techniques [10]. In the

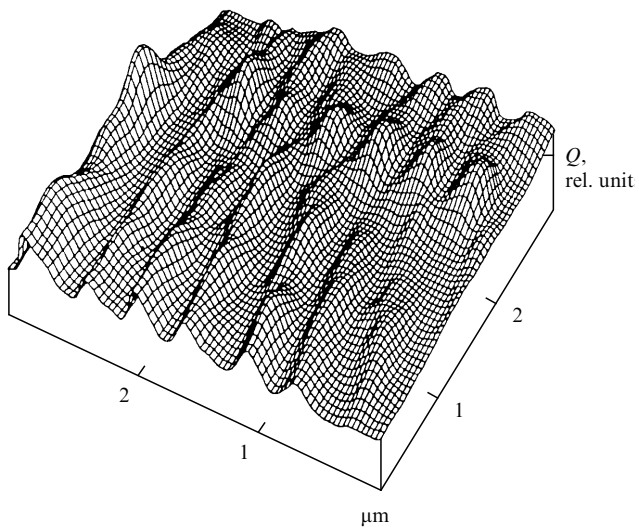

Figure 3. STS image (in terms of the parameter Q) of the surface conductivity of implanted Si after a pulsed interference laser annealing.

STM measurements they were most clearly discernible as a change in the parameter Q (Fig. 3), the period of such lattices being half that in their one-dimensional counterparts. Such two-dimensional structures have been known for quite a long time [11] and are believed to arise from the interference between the incident electromagnetic wave and the electromagnetic surface wave it generally excites in a metal (semiconductors are assumed to become metallic when melted by a laser beam). There exist, however, alternative models for the formation of such two-dimensional structures by a laser beam [11].

Local changes in the absorption and reflection coefficients during fixed depth evaporation provide the basis for binary information recording with a 0.8 – 1-μm-focused laser beam when manufacturing the optical memory disks. Due to its high mechanical and chemical resistance, the implantation-produced granular metallic film buried in the surface glass layer is very promising for the purpose [4]. The resolution power of such a detecting medium is as yet, however, unclear, because the randomly distributed optical absorption centres (metallic Fe particles) may be as large as tens of nanometers in diameter, leading to a nonuniform evaporation of the surface layer. Using interference laser evaporation to form a periodic submicron structure at the surface of the implanted glass, one can estimate the resolution power of such a detecting medium. Fig. 4 shows the AFM images of lattices formed at implanted Si and quartz-glass surfaces. Comparison shows that although the lattice on glass is of markedly lower quality than that on Si (because of the nonuniform evaporation of the metal-rich surface glass layer), still even on glass the lattices with a period of up to 1 μm are possible. This means that the resolution power of such a detecting medium reaches 1000 lines/mm, which is quite sufficient for its application as a mass-production laser-memory-disk matrix.

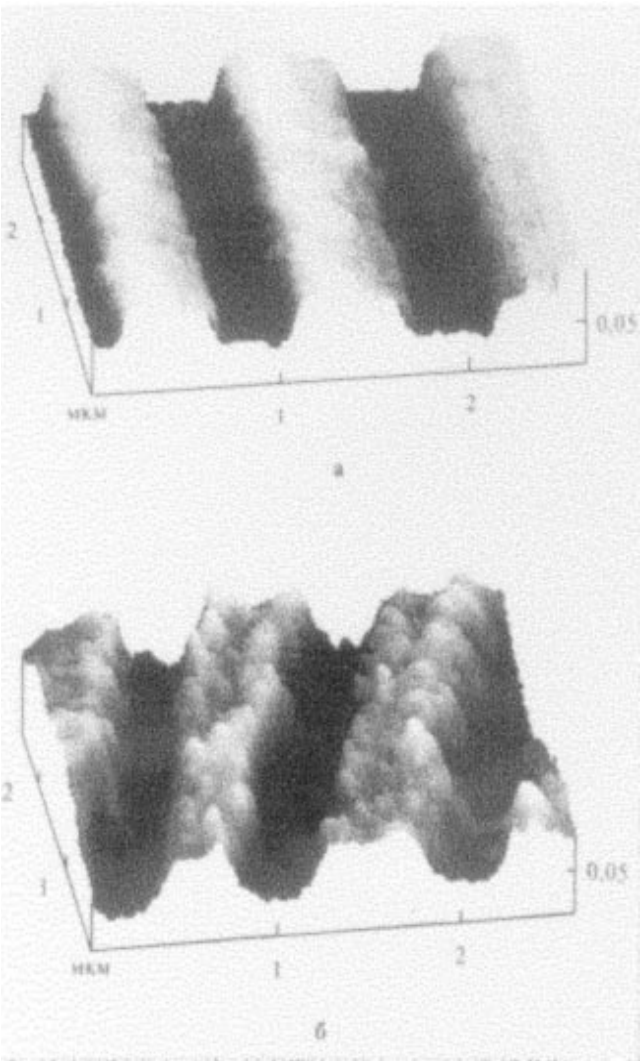

Figure 4. AFM image of one-dimensional periodic structures at the surface of implanted Si (a) and glass (b) formed by pulsed-interference laser evaporation.

4. Conclusions

With an STM as a means for controlling the cleanliness and passivation of the surface of a chemically active media, even measurements in air may provide reliable data on the microtopography and the electronic properties of the surface.

The current methods of electronic data processing make it possible to significantly reduce surface image distortions caused by the finite size and the shape of STM and AFM needles.

The high spatial resolution of STMs and AFMs makes it possible to study fine details of the light-surface interaction, in particular to investigate how the size of optical absorption centres affects the formation of a submicron periodic relief on the surface during its laser-stimulated local evaporation.

Finally, STS measurements allow a visualisation of one- and two-dimensional periodic conductivity variations produced by pulsed-interference laser annealing in a surface layer of Si.

The work has been supported in part by the Ministry of Science and Technological Policy of the Russian Federation (project No 143/57/4), and by the Academy of Sciences of Tatarstan (project No 04-12/95).

References

1. Bukharaev A A et al. *Poverkhnost'* **12** 69 (1994)
2. Bukharaev A A et al. *J. Vac. Sci. Technol. B* **13** 1274 (1995)
3. Bukharaev A A et al. *Fiz. Tverd. Tela* **33** 1018 (1991) [*Sov. Phys. Solid State*]
4. Certificate of Authorship 1231818 USSR *Patentnyi Bull.: Izobreteniya* **18** 256 (1995)
5. Bukharaev A A et al. *Pis'ma Zh. Tekh. Fiz.* **16** 8 (1990) [*JTP Letters*]
6. Bukharaev A A *Zavodskaya Laboratoriya* **10** 15 (1994)
7. Certificate of Authorship 4916118 USSR *Patentnyĭ Bull.: Izobreteniya* **44** 171 (1992)
8. Bukharaev A A et al. *Phys. Status Solidi A* **131** 79 (1992)
9. Bukharaev A A et al. *Poverkhnost'* **4** 104 (1993)
10. Bukharaev A A et al. *Opt. Spektrosk.* **79** 417 (1995) [*Opt. Spectrosc.* (Russia)]
11. Akhmanov S A et al. *Usp. Fiz. Nauk* **147** 675 (1985) [*Sov. Phys. Usp.* **28** (12) 1084 (1985)]

PACS numbers: **76.30.–v**, 76.30.Lh

An EPR study of the density of states and effective coupling constant in La_2CuO_4 doped with Sr or Ba

V E Kataev, Yu S Greznev, B Z Rameev, E F Kukovitskiĭ, G B Teitel'baum, M Breuer, N Knauf

Evidently, to verify an already existing or develop a new high-temperature superconductivity (HTSC) theory, it is essential to have experimental relations between the electronic parameters of the normal and superconducting states. In particular, it is undoubtedly of interest to examine the interrelation between the density of states of current carriers at the Fermi level $N(E_F)$ and the superconducting transition temperature T_c for various levels of the carrier concentration n in the system. In the present study we achieve this goal by using EPR on Gd^+ impurity ions to examine the electronic properties of La_2CuO_4 for various levels of strontium or barium doping. Thereafter, based on the obtained $N(E_F)$ and T_c dependences on n, it proves possible to analyse the behaviour of the effective coupling constant λ of the current carriers for various types of, and degrees of doping by, lanthanum oxides [1, 2].

It is known [3] that the spin relaxation of magnetic moments in metals is determined primarily by the exchange interaction with the conduction electrons (Korringa mechanism [5]). This manifests itself in the characteristic linear temperature dependence of the EPR line width ΔH, with a slope proportional to the square of the current carrier density of states $N^2(E_F)$. An earlier study of superconducting $La_{2-x}Sr_xCuO_4$ samples with an optimised strontium doping revealed that the EPR line width of Gd^{3+} impurity ions displays a linear Korringa behaviour over a wide range of temperatures [4]. This provided strong support to the notion that, even though somewhat off from the CuO_2 planes, which are the key lattice elements from the conductivity and superconductivity viewpoints, the spin probes implanted into the rare-earth positions do test the density of states in the conducting layers of the structure. The implication was that by studying the Korringa contribution of the Gd^{3+} spin probes to the line width as a function of the degree of substitution of bivalent strontium or barium for trivalent lanthanum in La_2CuO_4 (i.e., as a function of carrier concentration) one can monitor the variation of the density of states $N(E_F)$ over a wide region of the phase diagram for this metal oxide, and link this variation to the observed change in the critical temperature T_c.

The first part of the study consists of EPR experiments on polycrystal samples of $La_{1.99-x}Sr_xGd_{0.01}CuO_4$ ($0.08 \leqslant x \leqslant 0.35$). The dependence of the superconducting transition temperature T_c on strontium content in these samples is of bell-like form typical of this compound [6]. As the strontium (and hence current carrier) concentration is increased, T_c increases and reaches a maximum value of ~ 34 K at the superconductivity-optimising value of $x = 0.15$. As x is increased further, the T_c in the overdoped region decreases rapidly, and the samples with $x = 0.30$ and 0.35 do not become superconducting at all. The temperature dependence of the resistance $R(T)$ for samples with $x \leqslant 0.15$ is linear at high temperatures, which is typical of the HTSC materials. At low temperatures an additional, logarithmic contribution to $R(T)$ is seen, disappearing as the resistance vanishes on the superconducting transition. In the overdoped region ($x \geqslant 0.20$) the resistance follows the power law $\rho(T) \propto T^{1.5}$. In all of the samples studied, the EPR signal is the fine-structure spectrum of the Gd^{3+} ion. The entire extent of the spectrum is about 7 kOe, the most highly resolved components concentrating in the field range 1 – 3 kOe. Each component depends on both the temperature and the strontium content for its width. Due to the partial component overlap, only one — central — component yields the line width behaviour over the entire temperature range. The analysis of the spectrum was carried out with a special computer programme in which major spectral features were reproduced based on a simple, phenomenological and axially symmetric Hamiltonian with a fine-splitting parameter on the order of the Zeeman energy. For all the samples investigated there existed a sufficiently wide temperature range in which the line width $\Delta H(T)$ varied linearly, $\Delta H(T) = a + bT$. At low temperatures the samples with $x < 0.15$ acquired an additional logarithmic contribution to their line width, which correlated with a similar resistance behaviour. These features will be discussed in the second part of the study.

The linear temperature dependence of the EPR line width, $\Delta H(T) = a + bT$, implies that even though the local moments of Gd are located off the CuO_2 planes, there is a weak exchange coupling between them and the in-plane current carriers, permitting the spin probes to relax by the Korringa mechanism. The coefficient b (Korringa slope) for each component may (neglecting electron-electron interactions) be written as follows [3]:

$$b = 4\pi M^2 \left[N(E_F)\, J_{s,f}\right]^2, \text{ where } M^2 = S(S+1) - S_z(S_z+1)\,. \tag{1}$$

Here $J_{s,f}$ is the exchange integral between localised magnetic moments and conduction electrons, and M is the matrix element coupling the Gd^{3+} ion $|S_z\rangle$ state with its $|S_z - 1\rangle$ and $|S_z + 1\rangle$ states. The square of this matrix element also determines the corresponding transition probability and hence the resonance line intensity. An earlier estimate put $J_{s,f}$ at about 2.5 meV [4]. As EPR measurements indicate, changing strontium content (and hence the number of current carriers in the CuO_2 planes) alters the slope b in the $\Delta H(T)$ dependence. Since, according to (1), $N(E_F)$ is proportional to the square root of the Korringa slope b, the dependence of the density of states in $La_{2-x}Sr_xCuO_4$ on the strontium concentration x can be constructed. This dependence is shown in Fig. 1, in which the squares correspond to La_2CuO_4 samples doped with strontium. These points are fairly well approximated by the relationship $b^{1/2} = 2.89\,(x - 0.06)^{0.49}$ over the entire strontium concentration range.

Thus, both the critical temperature T_c and the density of states $N(E_F)$ turn out to be dependent of the strontium concentration. It is interesting to see how these quantities interrelate in various regions of the phase diagram of $La_{2-x}Sr_xCuO_4$. By eliminating the independent variable x from the experimental dependences $T_c(x)$ and $b(x)$ one can represent the critical temperature as a function of the inverse square root of the Korringa slope b for $La_{2-x}Sr_xCuO_4$. This dependence is shown by solid line in Fig. 2. As seen from the figure, except for the superconducting $x = 0.25$ and 0.28 samples, all other points form in these coordinates a nearly linear dependence, which [noting that b and $N(E_F)$ are related

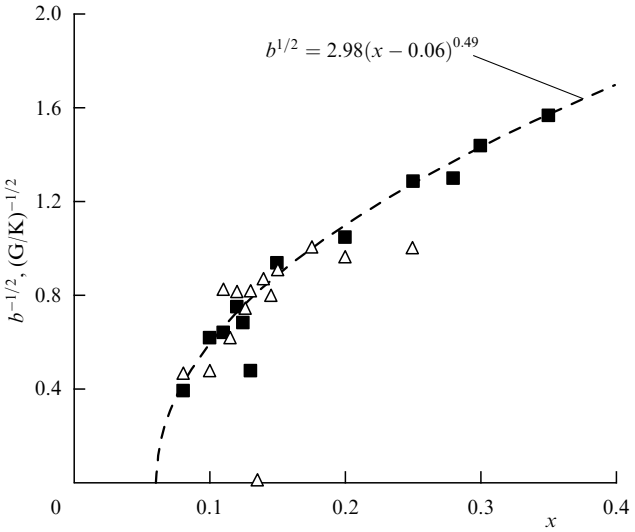

Figure 1. The dependence of the square root of the Korringa slope b upon the concentration of dopant M for $La_{1.99-x}Gd_{0.01}M_xCuO_4$ samples: ■ — M = Sr; △ — M = Ba.

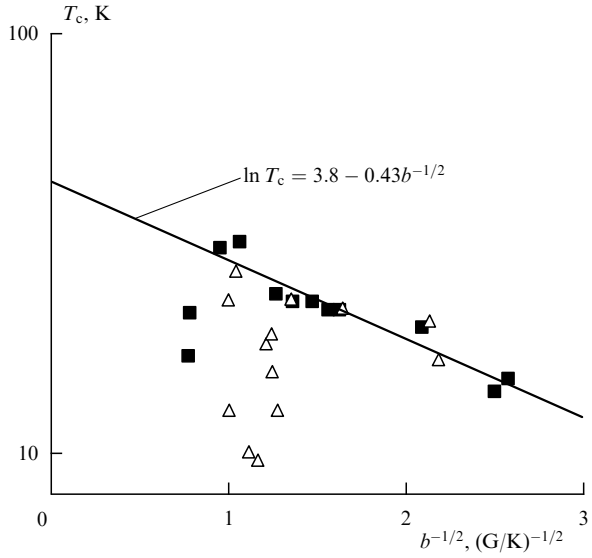

Figure 2. The dependence of the critical temperature T_c upon the Korringa slop b for $La_{1.99-x}Gd_{0.01}M_xCuO_4$ samples: ■ — M = Sr; △ — M = Ba. Solid line approximates experimental points (M = Sr or Ba) obeying the relationship $d[\ln T_c]/d[1/N(E_F)] = \text{const}$.

by (1)] thus relates the critical temperature and the density of states by

$$\frac{d[\ln T_c]}{d[1/N(E_F)]} = \text{const}\,, \tag{2}$$

yielding

$$T_c = \alpha \exp\left(-\frac{1}{\beta}\, b^{-1/2}\right), \tag{3}$$

where α and β are the fitting parameters. The experimental relationship between T_c and $N(E_F)$ thus obtained is reminiscent of the well-known BCS type critical temperature expression $T_c = \omega \exp(-1/\lambda)$, in which $\lambda = VN(E_F)$ is the effective coupling constant, V is the pairing potential, and ω, a certain characteristic frequency. Based on this expression and the measured data of Fig. 2 (squares), one can determine λ for each superconducting sample and estimate its dependence on the density of states $N(E_F)$ in $La_{2-x}Sr_xCuO_4$. Analysis showed that as b (and hence the density of states) increases, λ first grows, then reaches a maximum of ~ 2 for the superconductivity-optimum $x = 0.15$ sample, and then decreases rapidly for $x > 0.2$.

The growth of λ with increasing $N(E_F) \propto \sqrt{b}$ indicates the constancy of the pairing potential V for strontium dopings not exceeding the optimum value. At the same time, the rapid decrease in the coupling constant in the overdoped region in spite of the continuing growth of the density of states (Fig. 1) appears to indicate a sharp decrease of the pairing potential at high doping levels.

The second part of the study involves EPR experiments on polycrystalline $La_{1.99-x}Ba_xGd_{0.01}CuO_4$ samples and is primarily concerned with explaining the well-known effect of anomalous superconductivity suppression in $La_{2-x}Ba_xCuO_4$ in the narrow barium concentration range $x = 0.12-0.15$ [7]. This effect is linked to the structural transition from the orthorhombic (LTO) to the low-temperature tetragonal (LTT) phase occurring in the samples involved at $T < 70$ K, in the course of which the copper-oxygen octahedra alter their orientation in the superconducting planes [8]. The reason for this interrelation is not obvious, however, and may be of specifically HTSC origin.

$La_{1.99-x}Ba_xGd_{0.01}CuO_4$ samples with $x = 0.08-0.25$ were used in the study. The barium-content dependence of T_c in them had a characteristic 'ravine' feature at $0.12 \leqslant x \leqslant 0.15$, with T_c significantly reduced and even nonexistent (for $x = 0.135$) (Fig. 3). At high temperatures, sample resistance varied linearly with T. Below 100 – 150 K, it first saturated and then started to rise until the superconducting transition occurred. For the ravine edge samples (see Fig. 3) the resistance rise $\Delta\rho$ followed the law $\Delta\rho(T) \propto -\ln T$

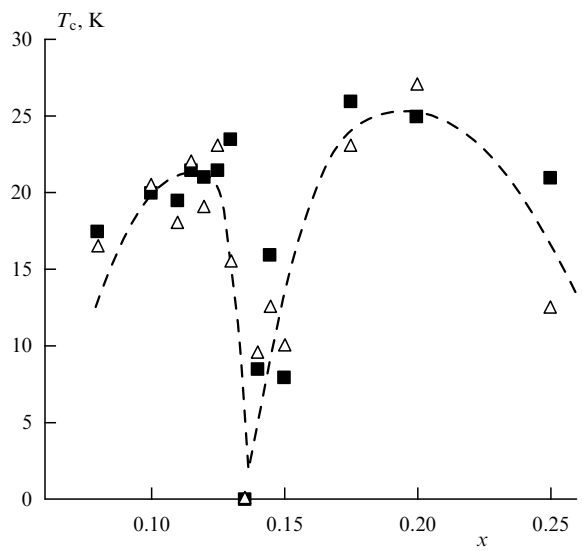

Figure 3. The dependence of the critical temperature T_c on barium content in $La_{1.99-x}Ba_xGd_{0.01}CuO_4$ samples, as measured from resistance (■) and microwave absorption in small magnetic fields (△). The dashed line is drawn only for ease of inspection.

similar to that in the $La_{2-x}Sr_xCuO_4$ system at low strontium-dopant levels. At the same time, for the ravine bottom samples the behaviour of $\Delta\rho(T)$ was closer to the exponential one, $\Delta\rho(T) \propto \exp(1/T^{1/4})$.

The EPR signal from $La_{1.99-x}Ba_xGd_{0.01}CuO_4$ samples was identical in most details to that of the fine structure of Gd^{3+} in the $La_{1.99-x}Sr_xGd_{0.01}CuO_4$ compound. There was, however, a distinguishing spectral feature of the $La_{1.99-x}Ba_xGd_{0.01}CuO_4$ samples with $0.12 \leqslant x \leqslant 0.15$, in that below 20 – 45 K additional lines, not describable by the fine-structure spin Hamiltonian, appeared. As in the case of the $La_{1.99-x}Sr_xGd_{0.01}CuO_4$ compound, for all of the samples the temperature dependences of the line width $\Delta H(T)$ were monitored for the central component of the spectrum. Its width followed the linear dependence $\Delta H = a + bT$ for $T > 60-100$ K, with the temperature slope b increasing monotonically with barium concentration x, except for the $x = 0.135$ sample for which $b = 0$. At $T < 60-80$ K, the line width exhibited an additional logarithmic contribution $\Delta H_{\log} = -C \ln T$, the value of C being maximum for the sample with a barium concentration close to $x = 0.135$.

If one takes the $\sqrt{b} \propto N(E_F)$ versus x plot previously given for $La_{2-x}Sr_xCuO_4$ and adds $La_{1.99-x}Ba_xGd_{0.01}CuO_4$ points to it, the two dependences appear to be very much the same (see triangles in Fig. 1). This indicates that the current carrier density of states in the CuO_2 planes is independent of the type of dopant. We can also take the dependence of T_c on $1/\sqrt{b} \propto 1/N(E_F)$ plotted earlier for the $La_{2-x}Sr_xCuO_4$ compound, and add the data obtained for barium doped La_2CuO_4 (triangles in Fig. 2). It is seen that the points for the superconductivity-critical barium concentrations $0.12 \leqslant x \leqslant 0.15$ depart significantly from relationship (2) obtained for the $La_{2-x}Sr_xCuO_4$ system. Whereas the points for samples outside this interval fall fairly well on this lanthanum-strontium straight line. Thus, the ravine in the dependence of $\ln T_c$ on $1/\sqrt{b}$ implies a decrease in λ in this barium concentration range, either because the low-temperature density of states are lower than that deduced from the high-temperature portions of the $\Delta H(T)$ dependence, or due to the reduction in the pairing potential V itself. Comparison of the EPR and resistance data implies the conclusion that a possible cause for this λ behaviour is a carrier localisation, which reduces the effective coupling constant by, for example, producing an energy spectrum pseudogap at the Fermi level, or enhancing the Coulomb repulsion due to reduced screening. Other possibilities are the logarithmic or exponential growth of low-temperature resistance, or EPR line broadening due to either the increased time of correlation between the current carriers and the Gd^{3+} spin moments, or the enhancement of spin fluctuations and the formation of local moments in CuO_2 planes in the localisation process. The additional EPR lines appearing in samples with $0.12 \leqslant x \leqslant 0.15$ at $T = 30-45$ K may indicate the formation of an internal field due (most likely) to spin-glass-type ordering of magnetic moments in the CuO_2 planes. It should be noted that the presence of short-range order at $T \sim 30$ K in $La_{2-x}Ba_xCuO_4$ compositions close to $x = 0.125$ has also been detected in NMR and μSR experiments [9].

The localisation effects observed at the same superconductivity-critical barium concentrations leading to the structural LTO-LTT transition in $La_{2-x}Ba_xCuO_4$ at $T < 70$ K suggests that carrier localisation is provoked by a structural instability. The more so that the structural transition is somewhat overextended in temperature and incomplete in volume [8], a factor which may produce real structure nonuniformities (phase separation) — most likely on a microscopic spatial scale. The phase separation assumption might also account for the magnetocorrelated regions observed in samples which still retain their superconducting properties.

Thus, based on the analysis of Gd^{3+} EPR experiments on the HTSC $La_{1.99-x}M_xGd_{0.01}CuO_4$ compound with various types and amount of bivalent substitutional ions (M = Ba, Sr), the following conclusions can be drawn:

— in the strontium- or barium-doped high-temperature superconductor La_2CuO_4, the critical temperature and the density of states at the Fermi level are related by a BCS type relationship. The behaviour of the effective coupling constant λ (rise with carrier concentration and a sharp decrease after the optimal concentration is reached) implies a significant reduction of the carrier-carrier attraction in the overdoped region of the phase diagram;

— the anomalous suppression of superconductivity in the $La_{2-x}Ba_xCuO_4$ compound in the barium concentration range $x = 0.12-0.15$ may be caused by the reduction in effective coupling constant due to the current carrier localisation resulting from a low-temperature structural instability. Samples of this stoichiometry may break up into superconducting and magnetocorrelated regions.

The work was supported by the State HTSC Research Programme Grant No 94045. The work of V E K and G B T was also supported by the International Science Foundation Grant NNX000. Part of the work was performed at the Cologne University under the special Deutsche Forschungsgesellschaft project SFB341.

References

1. Kataev V et al. *Phys. Rev. B* **48** 4030 (1993)
2. Rameev B et al. *Physica C* **246** 309 (1995)
3. Barnes S E *Adv. Phys.* **30** 801 (1981)
4. Kataev V E et al. *Pis'ma Zh. Eksp. Teor. Fiz.* **48** 433 (1988) [*JETP Letters* **48** 476 (1988)]
5. Korringa J *Physica* **16** 601 (1950)
6. Torrance J B et al. *Phys. Rev. Lett.* **61** 1127 (1988)
7. Moodenbaugh A R et al. *Phys. Rev. B* **38** 4596 (1988)
8. Axe J D et al. *Phys. Rev. Lett.* **62** 2751 (1989)
9. Tou H, Matsumura M, Yamagata H *J. Phys. Soc. Jap.* **62** 1474 (1993); Kumagai K et al. *J. Supercond.* **7** 69 (1994)